Available online at www.sciencedirect.com
SCIENCE DIRECT®
Journal of Theoretical Biology 233 (2005) 221–236
Journal of Theoretical Biology
www.elsevier.com/locate/yjtbi

Spatial models of virus-immune dynamics

Georg A. Funk[a,b,*], Vincent A.A. Jansen[a], Sebastian Bonhoeffer[b], Timothy Killingback[b]

[a]School of Biological Sciences, Royal Holloway-University of London, Egham (Surrey) TW20 0EX, UK
[b]Ecology and Evolution, Swiss Federal Institute of Technology (ETH) Zurich, CH-8092 Zurich, Switzerland

Received 30 July 2004; received in revised form 1 October 2004; accepted 4 October 2004
Available online 14 November 2004

Abstract

To date, the majority of theoretical models describing the dynamics of infectious diseases in vivo are based on the assumption of well-mixed virus and cell populations. Because many infections take place in solid tissues, spatially structured models represent an important step forward in understanding what happens when the assumption of well-mixed populations is relaxed. Here, we explore models of virus and virus–immune dynamics where dispersal of virus and immune effector cells was constrained to occur locally. The stability properties of our spatial virus–immune dynamics models remained robust under almost all biologically plausible dispersal schemes, regardless of their complexity. The various spatial dynamics were compared to the basic non-spatial dynamics and important differences were identified: When space was assumed to be homogeneous, the dynamics generated by non-spatial and spatially structured models differed substantially at the peak of the infection. Thus, non-spatial models may lead to systematic errors in the estimates of parameters underlying acute infection dynamics. When space was assumed to be heterogeneous, spatial coupling not only changed the equilibrium properties of the uncoupled populations but also equalized the dynamics and thereby reduced the likelihood of dynamic elimination of the infection. In line with experimental and clinical observations, long-lasting oscillation periods were virtually absent. When source–sink dynamics were considered, the long-term outcome of the infection depended critically on the degree of spatial coupling. The infection collapsed when emigration from source sites became too large. Finally, we discuss the implications of spatially structured models on medical treatment of infectious diseases, and note that a huge gap exists in data accurately describing infection dynamics in solid tissues.

Keywords: Mathematical models; Spatially structured models; Intra-host dynamics; Virus–immune dynamics; Dynamic elimination; Disease persistence

1. Introduction

Until recently, it was widely believed that some chronic infectious diseases such as those resulting from hepatitis B virus (HBV), hepatitis C virus (HCV), human immunodeficiency virus (HIV), human T-cell leukemia virus (HTLV), and human cytomegalo virus (CMV) are static infections (Pantaleo et al., 1993; Hengel et al., 1998; Emery et al., 1999). However, during the last decade this view has been superseded by a picture of highly dynamic infections, where production rates and clearance rates of viruses and of virus-infected cells appear to be on a time-scale of hours to days (Ho et al., 1995; Wei et al., 1995; Nowak et al., 1996; Nowak and Bangham, 1996; Zeuzem et al., 1996; Lam et al., 1997; Emery et al., 1999; Ramratnam et al., 1999). Instrumental in that shift of perspective were population dynamical models, which greatly improved our understanding of the replication dynamics of these viruses in vivo (Ho et al., 1995; Wei et al., 1995; Nowak et al.,

*Corresponding author. Tel.: +44 1784 414189; fax: +44 1784 470756.
E-mail addresses: georg.funk@rhul.ac.uk (G.A. Funk), vincent.jansen@rhul.ac.uk (V.A.A. Jansen), sebastian.bonhoeffer@env.ethz.ch (S. Bonhoeffer), tim.killingback@env.ethz.ch (T. Killingback).

0022-5193/$ - see front matter © 2004 Elsevier Ltd. All rights reserved.
doi:10.1016/j.jtbi.2004.10.004

1996; Nowak and Bangham, 1996; Payne et al., 1996; Phillips, 1996; Perelson et al., 1996, 1997; Zeuzem et al., 1996; Bonhoeffer et al., 1997; Lam et al., 1997; Neumann et al., 1998; Emery et al., 1999, 2002; Whalley et al., 2001).

Most of the modeling efforts to date assume panmictic (well-mixed) virus populations and describe spatially averaged infection dynamics at the whole-body level (reviewed in Nowak and May, 2000). However, the interaction between pathogens and the immune response tends to be local within the body of infected hosts. For example, it was recently shown that the assumption that HIV exists as a panmictic virus population was inconsistent with the pattern of genetic variation observed in solid tissues such as the spleen (Frost et al., 2001). Rather, the observations supported a picture of spatially structured populations consisting of a set of loosely coupled virus populations, also called "metapopulations" (Levins, 1969). Therefore, there is a need for spatially structured models to understand the consequences of spatial structure for virus dynamics in vivo.

In this paper, we have used two different types of spatially structured models to elucidate how local dispersal of virus and virus-specific immune cells influences infection dynamics and disease persistence in vivo. Our first model is a spatially extended version of the "basic" model of virus dynamics; the second, a spatially structured model that considers a localized virus-specific immune response. Both models are closely related to previously described models that do not consider spatial coupling (Nowak and Bangham, 1996). Because spatial heterogeneity is an important factor in population dynamics (for references see Dias, 1996), we also study the dynamics of each spatially structured model for the two cases of an entirely homogeneous and a heterogeneous environment. We discuss how the non-spatial models can be derived from spatially structured models, how predictions obtained from spatially structured models deviate from those obtained from non-spatial models, and what the implications for medical treatment are.

2. Models and results

In this paper we will discuss the following models: We first discuss model I(a), the "basic" model of virus dynamics. We next discuss model I(s), a spatially explicit extension of model I(a) that incorporates spatial spread of the virus. Model II(a) extends model I(a) by considering an immune response against virus-infected cells. Finally, model II(s) is a spatial extension of model II(a) that explicitly incorporates dispersal of virus and immune cells.

Model I(a): Basic model of virus dynamics

$$\begin{aligned}\dot{T} &= b - \mathrm{d}T - eTV,\\ \dot{Y} &= eTV - uY,\\ \dot{V} &= pY - cV.\end{aligned} \tag{1}$$

This model describes the interaction between a replicating virus and host cells in the simplest possible way and therefore does not consider any spatial structure. Due to its simplicity, it is referred to as the "basic" model of virus dynamics (Nowak and Bangham, 1996; reviewed in Nowak and May, 2000). Here, the variable T denotes the abundance of uninfected target cells, Y stands for the abundance of virus-infected cells that produce new virus particles, and V denotes the abundance of virus particles. The dot above a variable denotes the derivative of the respective variable with respect to time. Uninfected cells are produced at a constant rate b from a source (e.g. the thymus) and die at rate $\mathrm{d}T$. Hence, prior to infection, target cells are in a dynamical equilibrium given by $\hat{T}_0 = b/d$. Upon infection of uninfected cells with virus, infected cells are produced at rate eTV and die at rate uY. Free virus is produced from infected cells at rate pY and cleared from the system at rate cV. In a newly infected host, a virus particle infects on average $e\hat{T}_0$ target cells. These infected cells will, on average, live $1/u$ time units and will each produce p virus particles, which, on average, live for $1/c$ time units. The basic reproductive ratio, denoted by R_0, is therefore given by $bep/(duc)$. If $R_0 < 1$, the infection will only be transient and the system will eventually converge to its uninfected equilibrium (E0) with $\hat{T}_0 = b/d$ and $\hat{Y}_0 = \hat{V}_0 = 0$. If, on the other hand, $R_0 > 1$, then the system converges in damped oscillations to its infected equilibrium (E1) with $\hat{T}_1 = uc/(ep) = \hat{T}_0/R_0$, $\hat{Y}_1 = (bep - duc)/(eup)$, and $\hat{V}_1 = (bep - duc)/(euc)$ (Phillips, 1996; Nowak and Bangham, 1996). An example of the dynamics generated by this model is shown in Fig. 1 (solid line). A stability analysis for this model is given in Appendix A.

Model I(s): Spatially explicit basic model of virus dynamics

$$\begin{aligned}\dot{T}_{i,j} &= b - \mathrm{d}T_{i,j} - eT_{i,j}V_{i,j},\\ \dot{Y}_{i,j} &= eT_{i,j}V_{i,j} - uY_{i,j},\\ \dot{V}_{i,j} &= pY_{i,j} - cV_{i,j} - \frac{m_V}{8}\sum_{i_0=i-1}^{i+1}\sum_{j_0=j-1}^{j+1}[V_{i,j} - V_{i_0,j_0}].\end{aligned} \tag{2}$$

Model I(s) extends model I(a) by including spatial structure. Compared to model I(a) the newly introduced subscripts i and j refer to a site with grid coordinates i, j. We assumed a completely homogeneous environment in which all model parameters were the same at all sites. The additional term in the virus equation determines the spatial coupling. We assumed here that the local

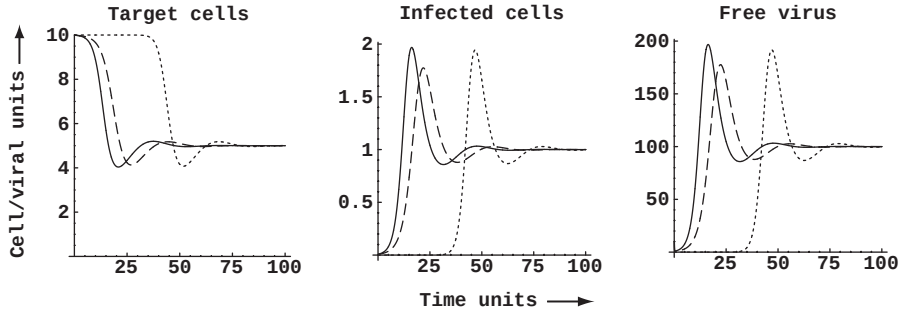

Fig. 1. Dynamics of target cells (left), infected cells (center), and virus (right). The solid line shows the solution of decoupled version of model I(s). The long-dashed line depicts the solution of model I(s) at the site of viral inoculum (11,11); the short-dashed line depicts the dynamics at a site close to the border (3,3). Viral export is set to 10%. Peak values of free virus are: 197 (solid line), 178 (long-dashed line), and 192 (short-dashed line). The delay between the solid line and the long-dashed line is ~5 time units, that one between the long-dashed line and the short-dashed line ~25 time units. The eigenvalue λ_{max} of the Jacobian of system I(s) is equal to $-9.77 \times 10^{-2} \pm 1.95 \times 10^{-1}\mathbf{i}$. It is virtually the same as for the non-spatial system I(a) (differences $<10^{-5}$). The negative real part indicates a damped dynamics. From the imaginary part follows an oscillation period P of ~32 time units ($P = 2\pi/\mathrm{Im}(\lambda)$). Parameters are as follows: $b=1$; $d=0.1$; $e=0.001$; $u=0.5$; $p=1000$; $c=10$. $T_0=10$, $R_0=2$, $\hat{T}_1 = 5$, $\hat{Y}_1 = 1$, and $\hat{V}_1 = 100$.

dynamics were coupled through the movement (diffusion) of virus to the eight nearest neighboring sites that surround the site where it emerged. Hence, m_V denotes the diffusion rate of free virus to adjacent sites. The stability analysis of model I(s) is given in Appendix A. Here, we emphasize that our qualitative results on the stability of model I(s) hold for almost all biologically plausible dispersal schemes, regardless of their complexity. This result derived in Appendix A holds as long as all eigenvalues of the matrix describing the geometrical interactions between grid sites are non-positive (see Appendix B). From Perron–Frobenius theory follows that this is the case for a large class of matrices (Minc, 1988). We used nearest neighborhood dispersal only for reasons of simplicity, as explained in the next paragraph.

Infection dynamics were described on a two-dimensional square grid with 21×21 sites. We assumed that the grid represents a small region of solid tissue, e.g. a thin section through parts of the liver, the spleen, or a lymph node. Target cells, such as liver hepatocytes or T cells of the lymphatic paracortical area (T-cell zone), were taken to be sessile. We further assumed that target cells were in steady state prior to infection and that there were no infected cells present. We started the infection in the center of the grid with an inoculum of 10 viral units. Since focal bursts of virions and foci of infected cells have been demonstrated in vivo around infected cells (Haase et al., 1996; Miller et al., 1997; Reinhart et al., 1998; Lau et al., 1999) and local viral replication followed by induction of local antiviral immunity occurs in vivo (Kaul et al., 2000; Ambrose et al., 2001), in each time unit a fixed percentage of virus (and in Appendix B of immune effector cells) were allowed to disperse into the eight nearest neighboring sites to that from which they emerged (up, down, left, right, and the four diagonals). In the literature, such a neighborhood is called the "Moore neighborhood" (Gaylord and Nishidate, 1996). Adoption of this rule ensured that dispersal of virus and immune effector cells was a local process.

Most of the simulations were done with periodic boundary conditions. These boundary conditions impose a toroidal topology on the grid, where opposite edges are joined in both dimensions. Thus, the same dispersal rules apply in the center and along the boundaries. Our choice of the grid size was—at least in part—motivated by the fact that besides the default periodic boundary conditions we also considered absorbing boundary conditions. Therefore, the grid had to be large enough to ensure that the loss of "material" along the borders did not affect the long-term outcome in the center of the grid. On the other hand, computational tractability put some constraints on the grid size as simulation time grew over proportional with increased grid size.

Due to a lack of reliable estimates of parameters for the within tissue dynamics, we selected the parameters used in this article to ensure that in equilibrium approximately one infected cell per site was present (range 0–15 cells site^{-1}). This is, for example, in line with the observed number of productively infected cells mm^{-2} in lymphoid tissues during primary SIVagm infection (Gueye et al., 2004). Nevertheless, numerical simulations in this paper should be regarded to illustrate qualitative spatial infection dynamics. To model infection dynamics in spatially heterogeneous tissues, parameters were allowed to vary uniformly within certain ranges.

2.1. Infection dynamics in a homogeneous environment

Let us now examine the infection dynamics generated by model I(s). First, we consider a completely homogeneous environment with identical parameter values for each site. Thus, the long-term outcome should be the same on each site. Initially, local populations of target

cells are assumed to be in steady state. We start the infection in the center of the grid with an inoculum of 10 viral units. The parameters are selected so that $R_0 > 1$ holds. We allow 10% viral export from any site into the eight nearest neighboring sites. This allows the infection to spread from the center over the whole grid. The long-dashed line in Fig. 1 shows the infection dynamics at the site of the viral inoculum, which has the grid coordinates (11,11). The short-dashed line in Fig. 1 depicts the dynamics on a site close to the border of the grid, which has the coordinates (3, 3). Due to viral diffusion, the peak of infection in the center (long-dashed line) increases delayed in time compared to the peak of a decoupled ($m_V = 0$) version of model I(s) (solid line) and it is also slightly damped. The virus load peak of the spatially structured model at the central site is 10% lower than that of the decoupled model (178 versus 197 viral units); the difference at the peripheral site is ~2.5% (192 versus 197 viral units). The higher peak virus load at the periphery is due to the fact that a peripheral site can have six adjacent sites at most, each with the same virus concentration as it has itself. Hence there is no net viral export to these sites. So, it may 'loose' only $\frac{2}{8} \times \frac{1}{10} = \frac{1}{40}$ or 2.5% of its virus concentration. The delay between the peak at the central site and the one on the border indicates that the infection travels over the grid with a speed of ~0.3 grid sites per unit of time. Taken together, one can see that the system converges on each site in damped oscillations toward the equilibrium (E1). At equilibrium, dispersal from and to local sites is in balance and does not alter the equilibrium properties of the local populations. Because (E1) represents the local as well as the spatially averaged infected equilibrium, the 'basic model of virus dynamics' serves as a good approximation for the spatial infection dynamics close at equilibrium. But are the two models also equivalent at the beginning of an infection, i.e. during the acute phase?

Fig. 2 indicates that model I(a), the basic model of virus dynamics, may not always serve as a good approximation for infection dynamics. Although it gives almost identical results as model I(s) at the very beginning of an infection, i.e. identical initial up-slopes, it may not be appropriate for obtaining parameter estimates at around the peak of the infection. Here it is worth noting that, in line with experimental results (Nowak et al., 1997; Little et al., 1999), the spatial model indicates a biphasic up-slope of the virus load curve (dashed line) while the non-spatial model lacks to reproduce this (solid line). The subdued viral growth rate is due to the fact that the infection settles to its equilibrium earlier at those sites where it started than in the periphery. Averaging out over all sights eventually results in a biphasic up-slope. Hence, it is worth noting that parameter estimates derived by fitting model I(a) to virus load data obtained from blood samples of patients,

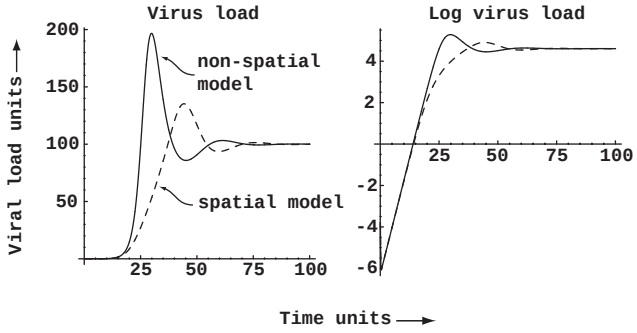

Fig. 2. Non-spatial and spatially averaged virus dynamics on a linear (left) and logarithmic (right) scale. The solid line shows the virus dynamics according to model I(a). The dashed line indicates the virus dynamics of model I(s) averaged out over the entire grid. Although both models have identical initial up-slopes and converge to the same steady-state virus load, the picture indicates a substantial deviation of the dynamics created by the two models at peak of viremia. This can lead to systematic errors in the estimates of parameters underlying peak viral dynamics when fitted by a non-spatial model. The biphasic up-slope of model I(s) indicating a subdued viral growth rate results from a curtailed target cell availability in the center of the grid where the infection equilibrates, while in the periphery it still continues to reach previously uninfected sites. Viral inoculum of the non-spatial model: 10/441 viral units. All other parameters as in Fig. 1.

which reflect a spatially averaged situation at the whole-body level, may underestimate the true—read local—infection dynamics in vivo.

2.2. Infection dynamics in a heterogeneous environment

We now relax the assumption of a homogeneous environment and simulate infection dynamics on a heterogeneous grid. That means that each parameter is allowed to vary randomly from site to site within a certain range from a uniform distribution. In particular, we allow that R_0 is below unity at some randomly distributed sites. Due to spatial coupling, there is a constant net flow of viruses from sites with an $R_0 > 1$, sources, to sites with an $R_0 < 1$, sinks. Source sites allow for viral amplification and dissemination while sink sites do not permit viral amplification. Thus sources can maintain the infection, while sinks cannot maintain the infection in isolation. Fig. 3 serves as an example showing the infected equilibria of a decoupled ($m_V = 0$) version of model I(s) on a grid where 60% of the sites have an $R_0 > 1$. Here, R_0 ranges from 0.09 to 29 (median 1.14); it is 1.2 on the site where the infection starts. We will refer to that example in the following paragraphs when examining what happens if local diffusion of virus is "turned on". Intuitively, we expect that spatial coupling will have a smoothing effect. Variation in the source to sink ratio will be considered further below.

Let us now examine the effect of *weak* spatial coupling on infection dynamics and disease persistence (as measured by equilibrium densities of infected cells

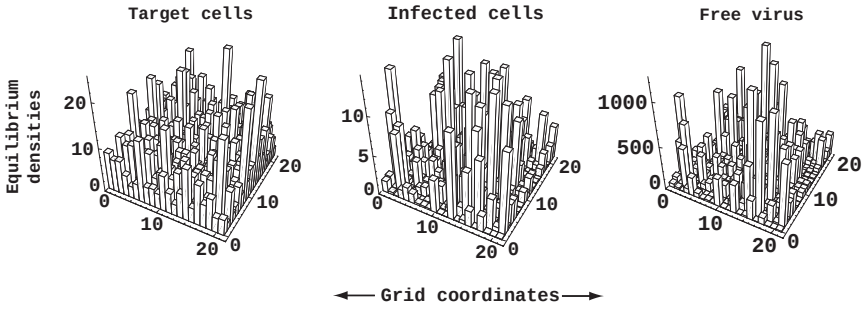

Fig. 3. Densities of target cells (left), infected cells (center), and virus (right) at equilibrium in a decoupled version of model I(s) on a heterogeneous 21×21 grid. R_0 ranges from 0.09 to 29 (median 1.14) and is >1 on 57% of the sites. Parameters are as follows (ranges): $b = 0.5$–1.5; $d = 0.05$–0.15; $e = 0.0005$–0.0015; $u = 0.1$–0.9; $p = 500$–1500; and $c = 10$–30 (uniform distributions).

and free virus) in vivo. To that end, we use the same initial grid configuration as in the previous paragraph, but now allow 1% of the virus to diffuse into the eight nearest neighboring sites. The results are summarized in Fig. 4. The top part of Fig. 4 shows that the virus (right) can achieve higher local densities than theoretically predicted by the non-spatial model while target cells (left) are below their predicted equilibrium value. The steady-state density of target cells at the site of infection is 13.75; R_0 at this site is 1.2. Thus, without spatial coupling, target cells would reach an equilibrium density of $\hat{T}_0/R_0 \approx 11.4$ units (Fig. 4, left, solid line). However, with 1% virus diffusion, the equilibrium density drops to ~9 units (long-dashed line). This indicates that, on a heterogeneous grid, spatial coupling and thereby introduced source–sink dynamics can change the equilibrium properties substantially. The short-dashed line in Fig. 4 depicts the dynamics on site (3, 3), which has a high R_0. Sites like this may export virus to nearby sites with lower equilibrium densities. The bottom of Fig. 4 shows how each site profits or loses from spatial coupling. To that end, we have calculated the local gains or losses by subtracting the equilibrium densities of the decoupled model (as shown in Fig. 3) from the equilibrium densities with 1% virus diffusion (not shown here).

Fig. 5 summarizes the effect of increasing spatial coupling on virus dynamics and the equilibrium density of free virus. The left side depicts how the dynamics of distant sites equalize with increasing spatial coupling (1%, 50%, 90% viral export) and that the initially differing abundances of virus tend toward an average (mean field) value. This is easy to understand if the virus load equation of (5) is re-written as follows:

$$0 = \dot{V}_{i,j} = pY_{i,j} - (c + m_V)V_{i,j} + m_V\bar{V}, \tag{3}$$

with $\bar{V}$ referring to the average neighborhood virus load. Hence,

$$V_{i,j} = (pY_{i,j} + m_V\bar{V})/(c + m_V). \tag{4}$$

The second term in the numerator, $m_V\bar{V}$, indicates that, with increasing spatial coupling, the average virus load of neighboring sites contributes more and more to the equilibrium virus load of site i,j. The center of Fig. 5 depicts the equilibrium densities of virus on the grid. Increased spatial coupling leads to a pronounced smoothing effect. The right side shows the local gains and losses of virus due to various degrees of spatial coupling (influx from sites with a higher equilibrium density or efflux to sites with a lower equilibrium density). Local gains and losses are not symmetrical for intermediate to high degrees of spatial coupling. Rather, the losses of some sites appear to be substantial, while the gains of other sites are relatively small. An explanation for this phenomenon is given in the next section.

2.3. Variation in the source–sink ratio

In this paragraph, we consider how variation in the fraction of sources to sinks, or in the quality of local sites, changes the long-term outcome of model I(s). Because virus load is the most important clinically monitored quantity of infected individuals, we focus here on its equilibrium density as an indicator of disease persistence. Fig. 6 depicts the relation between various degrees of virus diffusion and the cumulative equilibrium virus load over the whole grid for differing source–sink ratios. Spatial coupling does not significantly alter the equilibrium state as long as the fraction of sites that can maintain the infection is $>30\%$. Below 30%, however, long-term maintenance of the infection depends critically on the virus diffusion rate. Only for weak spatial coupling, which reduces the influence that nearby sink sites have on a source site, can the infection be maintained. For intermediate or strong spatial coupling, the sinks absorb the output of the sources more and more till they are finally annihilated. If, for example, $R_0 > 1$ holds on 10% of the grid and more than 50% of the virus from a source site is allowed to diffuse out, then the equilibrium property breaks down (for 55% viral export, less than one virus particle remains on the grid).

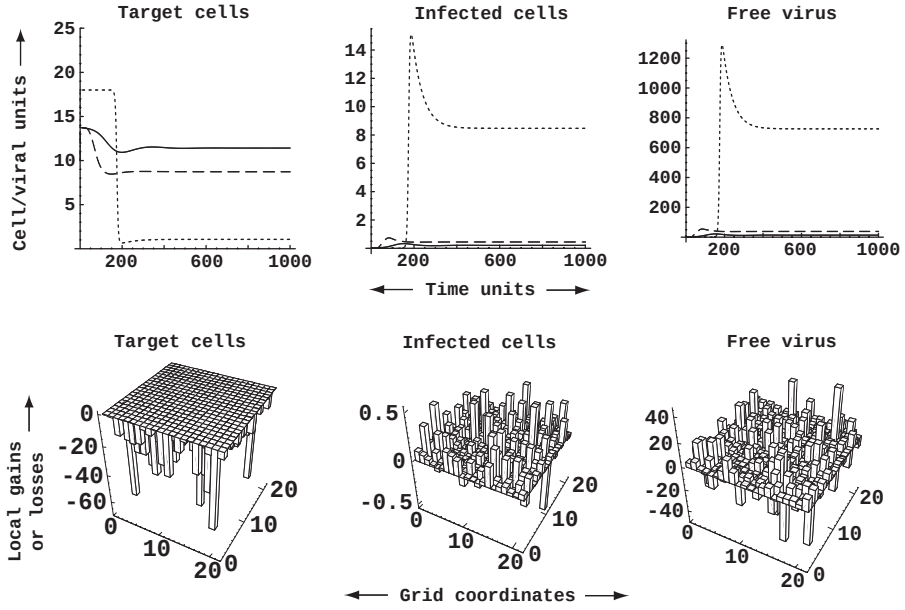

Fig. 4. Infection dynamics and relative gains or losses of target cells (left), infected cells (center), and virus (right) on a heterogeneous 21×21 grid. Top: Local dynamics of target cells, infected cells, and virus; bottom: local gains and losses for 1% viral export to the nearest neighboring sites according to model I(s). Parameters as in Fig. 3.

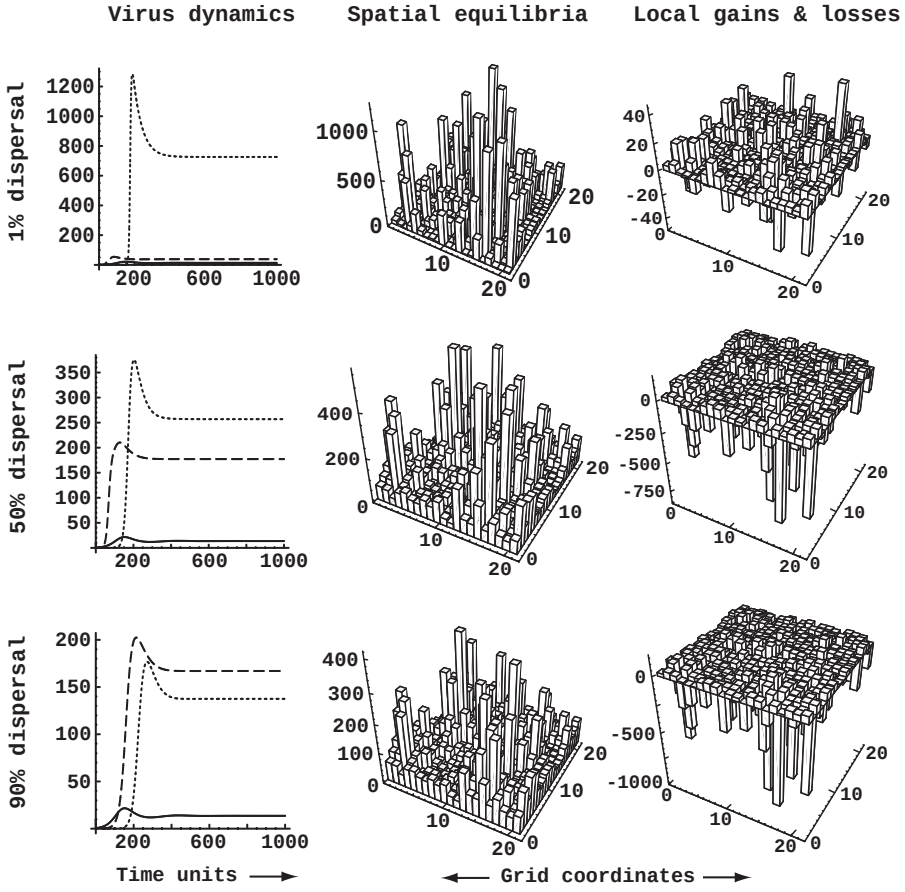

Fig. 5. Virus dynamics, equilibrium densities, and local gains and losses of virus for increasing spatial coupling. Top: 1% local dispersal of virus; middle: 50% local dispersal; and bottom: 90% local dispersal. Pictures on the left show that virus dynamics equalizes with increasing spatial coupling. Pictures in the center show the smoothing effect of increasing spatial coupling. Pictures on the right show that the local gains and losses are asymmetrical for high virus dispersal rates. Parameters as in Fig. 3.

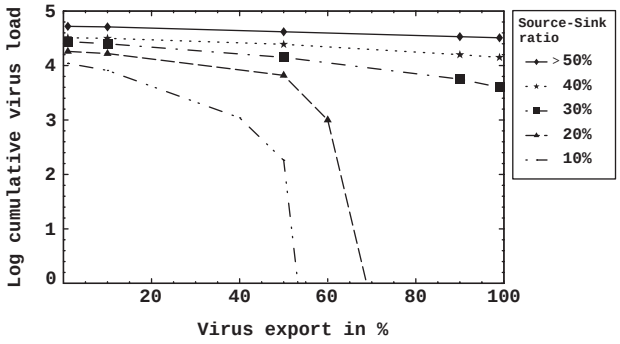

Fig. 6. Influence of the source to sink ratio and various degrees of spatial coupling on the long-term stability (persistence) of the infection. Log virus load indicates the cumulative virus load over the whole grid. Virus diffusion was increased stepwise from 1% over 10% up to 99% while reductions of the source to sink ratio from >50% to 10% (legend box) were achieved by varying the range of the parameter d from 0.05–0.15 to 0.2–0.3. The infection can only be maintained for weak spatial coupling. Intermediate or high degrees of spatial coupling allow the sinks erode and finally annihilate the sources. Parameters (except d) as in Fig. 3.

An intuition for the proposed collapse of the infection can be obtained from the following simplified model that considers only two qualitatively distinct types of patches. Here, the subscripts 1 and 2 refer to source and sink sites, respectively. They are linked throughout a pool of dispersers, i.e. $\bar{V} = fV_1 + (1-f)V_2$, where $\bar{V}$ denotes the average virus load and f denotes the fraction of sources in the system

$$\begin{aligned}
\dot{T}_1 &= b_1 - d_1 T_1 - e_1 T_1 V_1,\\
\dot{Y}_1 &= e_1 T_1 V_1 - u_1 Y_1,\\
\dot{V}_1 &= p_1 Y_1 - c_1 V_1 - m_V V_1 + m_V \bar{V},\\
\dot{T}_2 &= b_2 - \mathrm{d}_2 T_2 - e_2 T_2 V_2,\\
\dot{Y}_2 &= e_2 T_2 V_2 - u_2 Y_2,\\
\dot{V}_2 &= p_2 Y_2 - c_2 V_2 - m_V V_2 + m_V \bar{V}.
\end{aligned} \tag{5}$$

The equation describing virus dynamics at source sites reads as follows: virus is produced from infected cells at rate $p_1 Y_1$, cleared at rate $c_1 V_1$, emigrates at rate $m_V V_1$, and immigrates at rate $m_V \bar{V}$ from the pool of dispersers. The equation for the virus dynamics at sink sites reads similar. Using an invasion analysis, it can be shown that virus can increase when rare only if the uninfected side equilibrium is unstable, that is if

$$\begin{aligned}
&d_1 d_2 u_1 u_2 [-c_1 c_2 (R_0^1 - 1)(1 - R_0^2) - c_1 (R_0^1 - 1) f m_V\\
&\quad - c_2 (1 - R_0^2) m_V (f - 1)] < 0.
\end{aligned} \tag{6}$$

By using the above-introduced notation for sources and sinks, $R_0^1 > 1$ and $R_0^2 < 1$ holds, and condition (6) can be re-written as

$$\frac{1}{m_V} \frac{c_1 c_2 (R_0^1 - 1)(1 - R_0^2)}{-c_1 f (R_0^1 - 1) + c_2 (1 - f)(1 - R_0^2)} > 1. \tag{7}$$

Hence, if the diffusion rate m_V is too large the virus concentration cannot increase from small numbers. The reason for this is that at high diffusion rates of virus too much virus leaves source sites, in which it can increase, for sink sites where the numbers decrease.

In the remainder of the paper, we extend the basic model of virus dynamics by considering a specific immune response directed against virus-infected cells.

Model II(a): Virus–immune dynamics model

$$\begin{aligned}
\dot{T} &= b - \mathrm{d} T - eTV,\\
\dot{Y} &= eTV - uY - kXY,\\
\dot{V} &= pY - cV,\\
\dot{X} &= aXY - qX.
\end{aligned} \tag{8}$$

This model considers a specific immune response directed against virus-infected cells. It is an extension of model I(a). In addition to the three variables that were introduced there, the new variable X denotes the abundance of immune effector cells, e.g. virus-specific cytotoxic T-lymphocytes. Immune effector cells proliferate in response to an antigenic stimulus at rate aXY. They die at rate qX and kill infected cells at rate kXY (Nowak and Bangham, 1996; Callaway and Perelson, 2002). This system allows for three equilibria at most. First, the "naïve" or uninfected equilibrium (E0). Second, an infected equilibrium in the absence of an immune response, which is identical to (E1). Provided that the precursor frequency of immune cells is not zero and a minimum number of infected cells are around so that the growth condition for immune cells $a\hat{Y}_1 > q$ is fulfilled, an additional equilibrium (E2) exists where the pathogen can persist but is checked by a persisting immune response (Nowak and Bangham, 1996). The equilibrium (E2) is given by the following expressions: $\hat{T}_2 = bac/(epq + cad)$, $\hat{Y}_2 = q/a$, $\hat{V}_2 = pq/(ca)$, and $\hat{X}_2 = (abep - acdu - epqu)/(acdk + epqk)$ (Nowak et al., 1995; Nowak and Bangham, 1996). This equilibrium differs from (E1) in the following way: while the target cells go to a higher equilibrium value, the number of infected cells and of free virus is lower (Nowak and Bangham, 1996). The equivalent of a reproductive ratio in presence of an immune response, denoted by R_0^{IR}, can be defined. It is given by $bep/(cd(u + k\hat{X}_2)) = 1 + epq/(cad)$ (Nowak and May, 2000, p. 59). Because this value is always larger than unity, elimination of the virus is not possible.

The stability analysis of model II(a) is given in Appendix A, but local stability can also be evaluated via the eigenvalues of the Jacobian matrix. Here, for example, the maximum eigenvalue is negative, thus implying local stability. Compared to the maximum eigenvalue of model I(a), the real part of the maximum eigenvalue of model II(a) is an order of magnitude

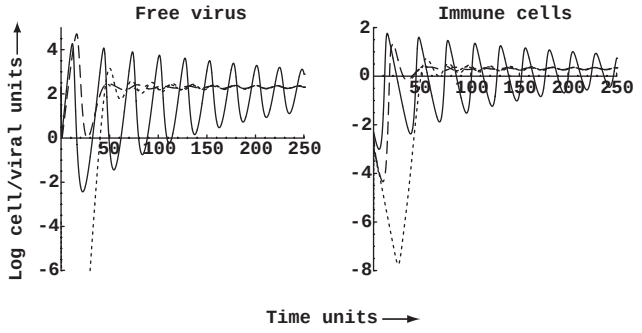

Fig. 7. Dynamics and convergence behavior of target cells, infected cells, free virus, and virus-specific immune cells for the first 250 time units on a log scale. The solid line depicts the dynamics of model II(a) that is without spatial coupling. The long-dashed line depicts the dynamics of model II(s) at the site of viral inoculum (11,11); the short-dashed line depicts the dynamics at site (3,3), which is close to the border of the grid. One can see that the presence of a spatial structure enhances population stability. The theoretically predicted equilibrium densities of target cells, infected cells, free virus, and immune cells are essentially reached after only one initial oscillation in the spatially structured model, while it takes several oscillations (>20) in the non-spatial model until the equilibrium is approached. The oscillation period is $\sim$22 time units. Parameters are as follows: $b=1$; $d=0.1$; $e=0.001$; $u=0.5$; $p=1000$; $c=10$; $a=2$; $q=0.2$; and $k=0.3$. Nearest neighboring dispersal of both viruses and immune cells is 10%. $R_0^{IR}=1.1$.

smaller, which explains why convergence toward the equilibrium (E2) occurs slower than in model I(a). The solid lines in Fig. 7 show the infection dynamics and the convergence behavior of target cells, infected cells, free virus, and immune cells for the first 250 time units.

Model II(s): Spatially explicit virus–immune dynamics model

$$\begin{aligned}
\dot{T}_{i,j} &= b - \mathrm{d}T_{i,j} - eT_{i,j}V_{i,j},\\
\dot{Y}_{i,j} &= eT_{i,j}V_{i,j} - uY_{i,j} - kX_{i,j}Y_{i,j},\\
\dot{V}_{i,j} &= pY_{i,j} - cV_{i,j} - \frac{m_V}{8}\sum_{i_0=i-1}^{i+1}\sum_{j_0=j-1}^{j+1}[V_{i,j} - V_{i_0,j_0}],\\
\dot{X}_{i,j} &= aX_{i,j}Y_{i,j} - qX_{i,j} - \frac{m_X}{8}\sum_{i_0=i-1}^{i+1}\sum_{j_0=j-1}^{j+1}[X_{i,j} - X_{i_0,j_0}].
\end{aligned} \tag{9}$$

Model II(s) is a spatial extension of model II(a). The interpretation of the notion of model II(s)—here given with fixed parameters—is the same as in model I(s). In simulations that considered a heterogeneous environment, the parameters were allowed to change from site to site. Again, we assumed that target cells and infected cells were sessile. The additional terms in the virus and the immune cell equation determine the spatial coupling. Here, local dynamics were coupled through movement (diffusion) of virus and immune effector cells to the nearest neighboring sites from which they emerged. The stability analysis of this model is presented in Appendix A. As we have already shown for model I(s), the stability properties of model II(s) hold as long as all eigenvalues of the connectivity matrix C are non-positive, which is the case for virtually all biologically plausible dispersal schemes.

2.4. Virus–immune dynamics in a homogeneous environment

We now compare the dynamics generated by model II(s) with those generated by model II(a). As in the previous section, we first consider a homogeneous environment. Initially, target cells are assumed to be in steady state. The initial densities of immune cells are given by random numbers ranging from 0 to 0.1, which reflects the variable frequency of precursor immune cells on each site. Thus, although the environment is homogeneous, the initial densities of precursor immune cells differ from site to site. Again, we start the infection with an inoculum of 10 viral units placed in the center of the grid. From there, it spreads over the whole grid (because R_0^{IR} is always >1) with a speed of $\sim$0.2 grid sites per unit of time. The maximal eigenvalue of the Jacobian of model II(s) is again complex ($\lambda = -5.1\times 10^{-3} \pm 2.9\times 10^{-1}\mathbf{i}$). Its negative real part indicates an attenuating wave, while its imaginary part indicates oscillations with a period of $2\pi/\mathrm{Im}(\lambda)\approx 22$ time units. Fig. 7 suggests that spatial coupling by local dispersal of virus and immune cells can enhance population stability by spatial averaging. Populations in the spatially structured environment equilibrate much faster ($\sim$10 times) than "isolated" populations. This is an interesting result, which deserves further investigation.

2.5. Dynamic elimination of a pathogen reconsidered

Focusing on the initial phase of the infection, Fig. 8 shows that infected cells and free virus fluctuate several

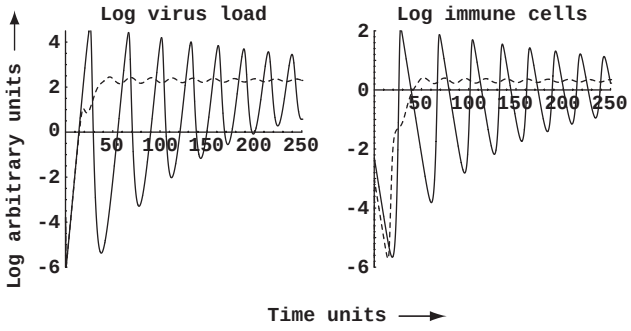

Fig. 8. Dynamic elimination of a pathogen. Solid line: model II(a); dashed line: model II(s). The inoculum size for model II(a) is rescaled so that both models have the same initial viral density. Spatial coupling by local dispersal of virus and immune effector cells reduces the likelihood that the pathogen will go extinct as a result of stochastic fluctuations with low magnitudes (dynamic elimination) at the beginning of the infection. This in turn enhances population stability and hence disease persistence in vivo. Parameters as in Fig. 7.

times down to low population densities (solid lines). Frequent oscillations with low magnitudes during the establishment of an infection carry the risk that the pathogen will go extinct as a result of stochastic fluctuations (i.e. dynamic elimination; Nowak and May, 2000, p. 63). The dotted lines in Fig. 8 show spatially averaged virus load and immune cell densities, respectively. Spatial coupling not only reduces the number of fluctuations but also their magnitudes. This increases the chance that the infection will persist in vivo. Efficient damping occurs because neighboring sites oscillate out of phase (here by a quarter of a period). In addition, virus diffusion to neighboring sites may bring the initial conditions closer to the equilibrium state.

2.6. Virus–immune dynamics in a heterogeneous environment

We now relax the assumption of a homogeneous environment and simulate the infection dynamics on a heterogeneous grid. As before, the parameters and therefore the R_0's are randomly chosen from site to site. However, because R_0^{IR} is always >1, the problem of source–sink dynamics does not exist here any more. Fig. 9 shows the long-term outcome of a *decoupled* version of model II(s). At the site where the infection starts, R_0 is 1.03. The figure shows that infected cells and virus exist on the whole grid. Immune cells, however, can co-exist only on those sites where infected cells are above a threshold density of 0.1 cells per site. This immune activation threshold is given by the term (q/a). The pattern of sites where the immune response persists versus other sites without immune cells is similar to the previously described source–sink pattern. Therefore, we examine in the next paragraph what happens if dispersal of both free virus and immune cells is "turned on".

Fig. 10 summarizes the effect of increasing spatial coupling of virus and immune cells on the long-term outcome of the infection. The left column shows the

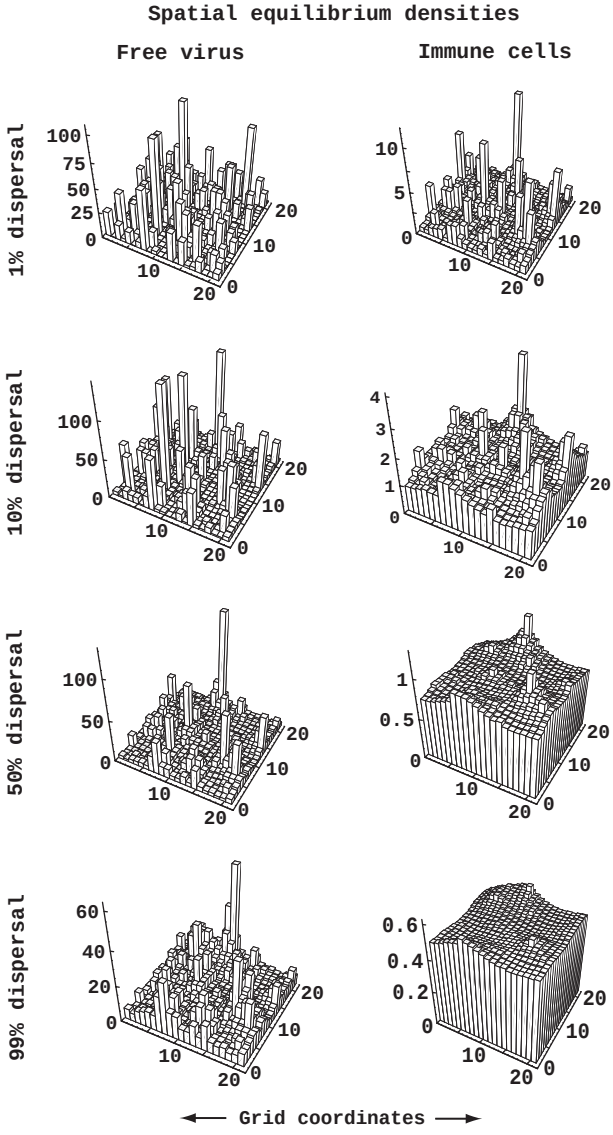

Fig. 10. Equilibrium densities of free virus (left) and immune effector cells (right) for increasing local dispersal. The smoothing effect of spatial coupling is more pronounced for the immune effector cells than for the virus. Nearest neighborhood coupling also seems to partially conserve spatial discontinuities of viral and host (tissue) factors. Parameters as in Fig. 9.

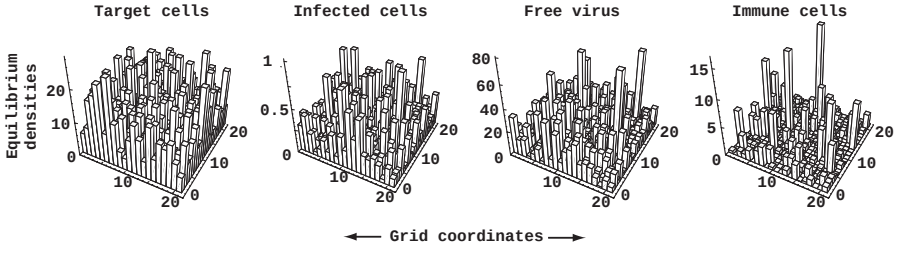

Fig. 9. Infected equilibrium densities of target cells, infected cells, virus, and immune cells according to a decoupled version of model II(s). Infected cells and virus can exist on each site of the grid. However, immune cells can only (co-)exist on those sites where infected cells achieve a certain threshold density. For the example shown here, a minimal density of 0.1 infected cells (q/a) is required to stimulate a local immune response. Parameters are as follows (ranges): $b=0.5$–1.5; $d=0.05$–0.15; $e=0.0005$–0.0015; $u=0.1$–0.9; $p=500$–1500; $c=10$–30; $a=0.5$–2.5; $q=0.1$–0.5; and $k=0.1$–10.6.

equilibrium density of virus, while the right column shows the equilibrium density of virus-specific immune cells. Dispersal of both virus and immune cells increases from 1% via 10% and 50% to 99%, respectively. As can be seen here, the smoothing (averaging) effect is stronger for the immune cells than for the virus. The local gains and losses are roughly symmetrical for target cells, infected cells, and viruses, while they are asymmetrical (with larger losses than gains) for the immune cells (data not shown here). This asymmetrical distribution of local gains and losses could partially be due to the fact that a certain threshold density of infected cells is required to stimulate a local immune response. Therefore, and in contrast to infected cells and virus, immune cells will be distributed with increasing dispersal over a larger fraction of sites where they did not exist before.

3. Summary and discussion

Compartmental analysis in biology and medicine has a long tradition (Anderson, 1983; Jacquez, 1985; Anderson and May, 1991). The majority of theoretical models in infection dynamics to date are based on the assumption of panmictic (well-mixed) virus and cell populations (Ho et al., 1995; Wei et al., 1995; Nowak and Bangham, 1996; Phillips, 1996; Perelson et al., 1996, 1997; Bonhoeffer et al., 1997; Nowak and May, 2000; Funk et al., 2001; Nowak et al., 1996; Whalley et al., 2001; Zeuzem et al., 1996; Lam et al., 1997; Neumann et al., 1998; Emery et al., 1999, 2002). Since most infections take place in solid tissues (Sprent and Tough, 1994; Haase et al., 1996; Chun et al., 1997; Miller et al., 1997; Grossman et al., 1998; Reinhart et al., 1998; Lau et al., 1999; Kaul et al., 2000; Ambrose et al., 2001; Frost et al., 2001), spatially structured models are an important step forward towards understanding what happens when the assumption of panmictic populations is abandoned. Here, we explored the consequences of incorporating spatial structure into models of virus and virus–immune dynamics. Our aim was to compare results obtained from models where dispersal of virus and immune effector cells was constrained to occur locally with results obtained from non-spatial models as described and studied in Nowak and Bangham (1996). In particular, we were interested in the question of whether the dynamics and stability properties of the non-spatial models were altered if spatial coupling was considered. It turned out that the two different types of models produced comparable results in some ways, but not in others. Because spatial heterogeneity is known to be an important factor in population dynamics (Dias, 1996), we also explicitly incorporated spatial discontinuities of viral and host factors in some of the simulations. The main features to note about the results are as follows (discussed thereafter):

(1) The stability properties of our spatial models hold for almost all biologically plausible dispersal schemes. It is sufficient that the all eigenvalues of the connectivity matrix are non-positive (Appendices A and B).
(2) In a homogeneous environment, the dynamics of the non-spatial model of virus dynamics deviate substantially from those of the spatially structured model at the peak of the infection. This deviation bears the risk of systematic errors in the estimates of parameters describing the early infection (Fig. 2).
(3) In a heterogeneous environment, weak spatial coupling by virus diffusion mainly changed the equilibrium properties of target cells (Fig. 4C). Increased spatial coupling was accompanied by a stronger equalization of the infection dynamics and a trend toward spatially averaged population densities (Fig. 5)
(4) Below a certain source to sink ratio, the long-term outcome of the infection turned out to depend critically on the degree of spatial coupling. The infection could not be maintained if the source sites were loosing too much virus by local diffusion (Fig. 6).
(5) The most noticeable property of the spatially extended virus–immune dynamics model was that long-lasting oscillations were virtually absent (Fig. 7). It equilibrated much faster than the non-spatial model and the risk of dynamic elimination of the pathogen (and the immune cells) during the invasion phase was markedly reduced.

Firstly, in Appendix A we show that the stability properties of our spatial models I(s) and II(s) are robust, as long as all eigenvalues of the connectivity matrix C describing viral dispersal or cell movements in vivo are non-positive. This covers virtually all biologically plausible dispersal schemes, regardless of their complexity. For reasons of simplicity and plausibility we used in our paper nearest neighborhood dispersal (discussed further below). But other dispersal schemes like dispersal via junctions to more distant sites may be considered as well if biologically justified.

Secondly, provided that the environment was entirely uniform, local diffusion of virus did change the local infection dynamics but not its long-term outcome when compared to the non-spatial model. The deviations observed at the beginning of the infection and around peak concentration of virus may lead to biased estimates of parameters underlying virus dynamics such as subdued viral growth rates. To avoid such systematic errors in parameter estimates, we suggest that spatially structured models (e.g. Zorzenon dos Santos and Coutinho, 2001 or Strain et al., 2002) should be used

when exploring the infection dynamics in solid tissues. Nevertheless, the basic model of virus dynamics may serve as a good approximation for the infection dynamics in solid tissues once a quasi-steady-state virus load has been approached.

Thirdly, if we relaxed the assumption of a homogeneous environment, then a small amount of spatial coupling did not alter the equilibrium properties much. This result follows rigorously from a general perturbation theorem given in Levin (1974), which can be used to derive the long-term outcome of model I(s) from model I(a). So, when mirroring the highly organized microstructure of some tissues (Cheynier et al., 1994; Gratton et al., 2000; Ambrose et al., 2001), then the main influence of weak spatial coupling was on the target cell population. Although the target cells were generally reduced, abundances of infected cells and free virus were not much increased. A possible explanation for the marked reduction of target cells on some sites could be source–sink dynamics that might have pushed local populations of target cells out of their respective uninfected equilibrium. With increased spatial coupling the dynamics of local sites started to equalize and the long-term outcome tended toward spatially averaged population densities. However, spatially averaged population densities within a tissue may still differ from the (panmictic) situation in the blood, which, for example, interconnects the whole system of lymphoid tissues and therefore may reflect averages on a macroscopic size scale.

Fourthly, if the source sites were clearly outnumbered by sink sites, then stability critically depended on the degree of spatial coupling. The system broke down if more than 50% of the virus that emerged from a site diffused away. The abrupt (nonlinear) decline in the virus load over a narrow range of diffusion could be due to the fact that the frequent sinks "sucked off" too much virus from the rare randomly distributed (and therefore largely isolated) sources. In addition, it is worth noting that the mean R_0 averaged across the grid was >1, while the R_0 calculated from averaged parameter values was <1. Therefore, it is possible that with increased spatial coupling the system was shifted toward a state that was characterized by the "averaged parameter dynamics". However, as soon as $R_0<1$ was achieved (corresponding to a kind of phase transition), the nonlinear response of the system to spatial coupling caused it to collapse. The observation that disease persistence depended critically on virus diffusion once a low source to sink ratio (virus load) was achieved may inspire novel strategies to eradicate some chronic infections such as HBV or HIV.

Clearly, the grid design of our spatial models serves as a simplified starting point and does by no means rule out more complex patterns of spatial interactions. Here, we briefly discuss in as how far our assumption is justified that viruses and cells disperse locally. Some early HIV studies contain spectacular electron micrographs showing directed shedding of HIV virions (Bourinbaiar and Phillips, 1991; Tan et al., 1993), while a recent review by Johnson and Huber (2002) states that a number of animal viruses, including HIV, have become adept to move from an infected cell to an adjoining uninfected cell, e.g. by cell junctions. In tissues, diffusion of virions via the interstitium away from a source of infection is primarily a local process, while paracrine secretion of cytokines from an infected cell may activate nearby cells thus rendering them susceptible for de novo infection. Although less is known about immune cell trafficking in vivo, recent studies using advanced imaging techniques seem to back our local motion approach (Mandl et al., 2002; Tibaldi et al., 2002; Huang et al., 2004).

To date, estimates of efficacies of antiviral drugs in vivo are based on basic reproductive ratios that were obtained from non-spatial (panmictic) models (Perelson et al., 1996, 1997; Bonhoeffer et al., 1997; Neumann et al., 1998; Emery et al., 1999; Little et al., 1999; Whalley et al., 2001; Callaway and Perelson, 2002; Funk, 2003). However, as we showed here, although non-spatial models predict extinction of the infection, spatially structured models instead predict persistence of the infection for intermediate dispersal rates. Since accurate estimations of basic reproductive ratios are of considerable importance in clinical evaluations of drug efficacies, it seems likely that more refined estimates of basic reproductive ratios in the future will depend significantly on results obtained from spatially structured models. Therefore, current predictions based on non-spatial models regarding the eradication of viral infections such as HIV, HBV, HCV, or CMV in vivo should not be taken to be definitive.

Fifthly, it was interesting to see that the same dynamics that occasionally brought pathogen populations to dynamic elimination in some non-spatial virus–immune dynamics models was able to enhance population stability and hence disease persistence when spatial coupling was considered in those models. This was mainly due to the fact that neighboring sites oscillated with an appropriate phase shift (here with a quarter of an oscillation period), which efficiently damped the magnitude of the oscillations. We could also show that the spatially structured model equilibrated much faster ($\sim$10 times) than its non-spatial analogue. In addition to the phase shift, quick virus diffusion after "inoculation" could have changed the initial conditions by pushing the whole system closer to its equilibrium. We also conducted simulations with artificial local extinction thresholds to test whether this would alter the long-term outcome of the infection. However, it turned out that spatial coupling damped the system so efficient that local extinction could only be

achieved for relatively high quasi-extinction thresholds ($\geqslant 5\%$ of the equilibrium value), which appear not to be realistic. Noteworthy, increased overall population persistence has also been found in host–parasitoid models with restricted local dispersal of parasites and hosts (Hassell et al., 1991).

Although there may be other (non-spatial) models that may be less oscillatory, our findings are novel and in contrast to the previously postulated "dynamic elimination" hypothesis. It is worth noting that the theoretically predicted phenomenon of dynamic elimination of a pathogen has been viewed as controversial by physicians. The observations obtained from our spatially structured model, however, allow us to reinterpret dynamic elimination as being essentially an artifact of non-spatial modeling (Wodarz et al., 2000; Nowak and May, 2000). When considering spatial structure in the numerical simulations, we observe a substantial reduction in the risk of dynamic elimination of a pathogen, and the model is also much less oscillatory. This is, for example, in line with data obtained from acute SIV- and HIV-infected individuals, where the virus load approaches the viral set point without extensive oscillations (Nowak et al., 1997; Little et al., 1999; Lindback et al., 2000). Thus, spatially structured models have the potential to reconcile theoretically obtained predictions based on non-spatial models with experimental/clinical observations. A nice example where dynamic elimination seems to fit the biology is given in Payne et al. (1996).

Finally, it is worth noting that the specific type of spatial coupling by nearest neighborhood dispersal, which efficiently attenuated the influence of nearby sites with distance, partially conserved spatial discontinuities of viral- and host-mediated factors. To ensure that our results were not confounded by the choice of periodic boundary conditions, we repeated with both spatial models a number of simulations using absorbing boundary conditions. We surrounded the 21×21 grid with a belt of "black-hole" sinks (sites that can only absorb) and observed what happened in the center of the grid and at the periphery. It turned out that absorbing boundary conditions sucked off "material" (cells and viruses) from about three rows/columns and thereby changed the dynamics and equilibria of these sites along the border. However, the majority of the sites within the grid were not affected by absorbing boundary conditions and in general the results were very similar to the simulations with periodic boundary conditions.

We conclude this article by emphasizing that spatially structured models are essential in improving our understanding of the dynamics of viral infections in vivo and in accurately predicting the drug efficacies required to eradicate them. We note that there currently exists a huge gap in data satisfactorily describing infection dynamics in solid tissues.

Acknowledgements

We thank Robert H.J. Payne and two anonymous referees for comments on the manuscript. We gratefully acknowledge financial support from the Swiss National Science Foundation. G.A.F. was partially supported by a Marie Curie fellowship from the European Community, Brussels, through Contract No: MEIF-CT-2004-501039. Parts of this work were presented at the 11th International Workshop on HIV Dynamics and Evolution, Stockholm, Sweden, 2004.

Appendix A. Stability analysis of spatial and non-spatial models

A.1. Local stability of model I(a)

The local stability of a model such as model I(a) may be determined from the Jacobian matrix. The Jacobian of model I(a) evaluated at the infected equilibrium (E1) is given by the matrix

$$J = \begin{pmatrix} -d - e\hat{V}_1 & 0 & -e\hat{T}_1 \\ e\hat{V}_1 & -u & e\hat{T}_1 \\ 0 & p & -c \end{pmatrix} = \begin{pmatrix} -d - (R_0-1)/(uc) & 0 & -be/(\mathrm{d}R_0) \\ (R_0-1)/(uc) & -u & be/(\mathrm{d}R_0) \\ 0 & p & -c \end{pmatrix}. \quad \text{(A.1)}$$

The characteristic equation of the Jacobian (2) follows from $\mathrm{Det}[J - \lambda I] = 0$, where I is the identity matrix. It can be brought to the normal form $\lambda^3 - a_1\lambda^2 - a_2\lambda - a_3 = 0$. Necessary and sufficient conditions for local stability of an equilibrium are provided by the Routh–Hurwitz criteria. These stability criteria put constraints on the coefficients a_1, a_2, and a_3, i.e. $a_1 > 0$, $a_3 > 0$, and $a_1 a_2 > a_3$ (e.g. May, 1974, p. 196). Here, $a_1 = c + u + \mathrm{d}R_0$, $a_2 = (c+u)\,\mathrm{d}R_0$, and $a_3 = c\,\mathrm{d}u$. Since all parameters of our model are positive real numbers, $a_1 > 0$ and $a_3 > 0$ are always fulfilled. Substituting a_1, a_2, and a_3 by the right-hand side expressions of the above identities leads to

$$c^2\,\mathrm{d}R_0 + c\,\mathrm{d}^2R_0^2 + u^2\,\mathrm{d}R_0 + u\,\mathrm{d}^2R_0^2 + 2R_0c\,\mathrm{d}u > c\,\mathrm{d}u \quad \text{(A.2)}$$

for the third Routh–Hurwitz condition. This can be rewritten as

$$c^2\,\mathrm{d}R_0 + c\,\mathrm{d}^2R_0^2 + u^2\,\mathrm{d}R_0 + u\,\mathrm{d}^2R_0^2 + c\,\mathrm{d}u(2R_0 - 1) > 0. \quad \text{(A.3)}$$

The left-hand side remains positive for any $R_0 \geqslant \frac{1}{2}$. So, with positive real-valued parameters and $R_0 \geqslant 1$ (for $R_0 < 1$ $\hat{Y}_1$ and $\hat{V}_1$ were negative) the Routh–Hurwitz

criteria are always fulfilled, hence the infected equilibrium (E1) is always locally stable if it is positive.

A.2. Local stability of model I(s)

Following a method for linearized neighborhood stability analysis of metapopulation models (Jansen and Lloyd, 2000; Lloyd and Jansen, 2004), our $n \times n$ system I(s) can be decomposed into n^2 decoupled three-dimensional subsystems. After a similarity transformation outlined in Jansen and Lloyd (2000), the Jacobian of model I(s), which contains now the decoupled linearized equations describing the dynamics of a small perturbation around the infected equilibrium, is obtained by adding $m_V\mu_s$ to element 3,3 of the Jacobian of model I(a) (see above). Hence the Jacobian of model I(s) takes the form

$$J + \begin{pmatrix} 0 & 0 & 0 \\ 0 & 0 & 0 \\ 0 & 0 & m_V \end{pmatrix} \mu_s. \tag{A.4}$$

Here, μ_s denotes the submaximal eigenvalue of the matrix C describing the connectivity of the grid. The eigenvalues of the connectivity matrix C (see Appendix B) are

$$\mu_{kl} = 2(2\cos(2\pi k/n) + \cos(4\pi l/n) - 3), \tag{A.5}$$

with both $k, l = 0, 1, \ldots, n-1$. A general discussion of how to get the eigenvalues of the connectivity matrices for various neighborhood geometries can be found in Othmer and Scriven (1971). The eigenvalues of the Jacobian of model I(s) follow from the equation

$$\mathrm{Det}\left[J + \begin{pmatrix} 0 & 0 & 0 \\ 0 & 0 & 0 \\ 0 & 0 & m_V \end{pmatrix} \mu_s - \lambda I \right] = 0. \tag{A.6}$$

The coefficients of the characteristic equation have the same form as for the non-spatial model, i.e. $a_1 = \tilde{c} + u + \mathrm{d}R_0$, $a_2 = (\tilde{c} + u)\,\mathrm{d}R_0$, and $a_3 = \mathrm{d}u\tilde{c}$, with $\tilde{c} = c - m_V\mu_s$. Using the same arguments as before (i.e. positive real-valued parameters, constraints on a_1, a_2, and a_3, and $R_0 \geqslant 1$), it is easy to show that the Routh–Hurwitz criteria are always fulfilled if $\tilde{c} > 0$. Since $m_V \geqslant 0$ and $\mu_s < 0$, $\tilde{c} > 0$ always holds. Therefore, symmetry breaking, i.e. instability due to spatial interactions, cannot occur. Note that all elements of matrix C are non-negative if a suitable number is added to all diagonal elements. If the resulting matrix is irreducible it follows from Perron–Frobenius theory that there is at most one positive eigenvalue (Minc, 1988). As a corollary it follows that all eigenvalues of C are non-positive if C is irreducible (Lloyd and Jansen, 2004). As a consequence, all eigenvalues of C are non-positive (see Appendix B).

A.3. Local stability of model II(a)

The characteristic equation of model II(a) takes the form $\lambda^4 - a_1\lambda^3 - a_2\lambda^2 - \lambda a_3 - a_4 = 0$. The Routh–Hurwitz criteria again provide necessary and sufficient conditions for an equilibrium to be locally stable. The following constraints on the coefficients a_1, a_2, a_3, and a_4 have to be fulfilled: $a_1 > 0$, $a_3 > 0$, $a_4 > 0$ and $a_1a_2a_3 > a_3^2 + a_1^2a_4$ (May, 1974, p. 196). Here,

$$a_1 = c + u + \mathrm{d}R_0^{IR} + u(R_0 - R_0^{IR})/R_0^{IR},$$

$$a_2 = \mathrm{d}uR_0 + c(u + \mathrm{d}R_0^{IR}) + [u(R_0 - R_0^{IR})(c + q)/R_0^{IR},$$

$$a_3 = \mathrm{d}u(cR_0 + q(R_0 - R_0^{IR})) + [u(R_0 - R_0^{IR})(cq)]/R_0^{IR},$$

and

$$a_4 = c\,\mathrm{d}qu(R_0 - R_0^{IR}).$$

Since R_0^{IR} is always >1 and all parameters of our model are positive real numbers, $a_1 > 0$, $a_2 > 0$, $a_3 > 0$, and $a_4 > 0$ are fulfilled if $R_0 > R_0^{IR}$. The fourth Routh–Hurwitz criterion comes down to: $((R_0^{IR})^3/(uR_0))(c + \mathrm{d}R_0^{IR})(c^2R_0^{IR} + qu(R_0 - R_0^{IR}) + cuR_0)(\mathrm{d}(R_0^{IR})^3 + qu(R_0 - R_0^{IR}) + \mathrm{d}uR_0R_0^{IR}) > 0$. It is always fulfilled as long as $R_0 > R_0^{IR}$ holds, hence the infected equilibrium (E2) is always locally stable if it exists and if it is positive.

A.4. Local stability of model II(s)

Following the same procedure for linearized neighborhood stability analysis as for model I(s), the determinantal equation that leads to the eigenvalues of the Jacobian of model II(s) is given by the expression

$$\mathrm{Det}\begin{bmatrix} -\lambda - d - e\hat{V}_2 & 0 & -e\hat{T}_2 & 0 \\ e\hat{V}_2 & -\lambda - u - k\hat{X}_2 & e\hat{T}_2 & -k\hat{Y}_2 \\ 0 & p & -\lambda - c + m_V\mu_s & 0 \\ 0 & a\hat{X}_2 & 0 & -\lambda + m_X\mu_s \end{bmatrix} = 0. \tag{A.7}$$

The coefficients of the characteristic equation have the same structure as for the non-spatial model, i.e.

$$a_1 = \tilde{c} + \tilde{q} + u + \mathrm{d}R_0^{IR} + u(R_0 - R_0^{IR})/R_0^{IR},$$

$$a_2 = \tilde{c}\tilde{q} + \mathrm{d}uR_0 + (\tilde{c} + \tilde{q})(u + \mathrm{d}R_0^{IR}) + [u(R_0 - R_0^{IR})(\tilde{c} + \tilde{q} + q)]/R_0^{IR},$$

$$a_3 = \tilde{c}\tilde{q}(u + \mathrm{d}R_0^{IR}) + \mathrm{d}u(R_0(\tilde{c} + \tilde{q}) + q(R_0 - R_0^{IR})) + [u(R_0 - R_0^{IR})(\tilde{c}\tilde{q} + \tilde{c}q)]/R_0^{IR},$$

and

$$a_4 = \mathrm{d}u(\tilde{c}\tilde{q}R_0 + \tilde{c}q(R_0 - R_0^{IR})),$$

with $\tilde{c} = c - m_V\mu_s$ and $\tilde{q} = -m_X\mu_s$. It is worth noting that the (negative) eigenvalue μ_s of the connectivity matrix C, which appears in both dispersal terms, is the same as for model I(s) because the geometry of the neighborhood remains the same. We have further set $m_V = m_X$.Thus, one can follow the procedure outlined for model II(a) to evaluate local stability of model II(s). The fourth Routh–Hurwitz criterion can be re-written as $a_1a_2a_3 - a_3^2 - a_1^2a_4 > 0$. Substituting in the respective expressions from above for a_1, a_2, a_3, and a_4, and neglecting the common positive factors, $(R_0^{IR})^3/(uR_0(uR_0 + \tilde{q}R_0^{IR}))$, the following expression can be obtained after some algebraic transformations (here done with a program for formula manipulation):

$$\begin{aligned}
&[\mathrm{d}(R_0^{IR})^2(\tilde{q} + \mathrm{d}R_0^{IR}) + u((R_0 - R_0^{IR})(q + \tilde{q})\\
&\quad + R_0^{IR}(\tilde{q} + \mathrm{d}R_0))][\tilde{c}^2R_0^{IR}(\tilde{c} + \tilde{q} + \mathrm{d}R_0^{IR})\\
&\quad + u(\tilde{c}^2R_0 + \mathrm{d}R_0^{IR}(q(R_0 - R_0^{IR}) + \tilde{q}R_0))]\\
&\quad + \tilde{c}\{\mathrm{d}^2\tilde{q}(R_0^{IR})^4(\tilde{q} + \mathrm{d}R_0^{IR}) + \mathrm{d}u(R_0^{IR})^2\\
&\quad \times [2\tilde{q}(q + \tilde{q})(R_0 - R_0^{IR}) + \mathrm{d}qR_0^{IR}(R_0 - R_0^{IR})\\
&\quad + R_0^{IR}(2\tilde{q}^2 + 3\mathrm{d}\tilde{q}R_0 + \mathrm{d}^2R_0R_0^{IR})]\\
&\quad + u^2[(q + \tilde{q})(R_0 - R_0^{IR}) + R_0^{IR}(\tilde{q} + \mathrm{d}R_0^{IR})]^2\} > 0. \qquad \text{(A.8)}
\end{aligned}$$

One can see from this formula that it always takes positive values provided that $R_0 > R_0^{IR}$ holds. So, together with the other three necessary conditions, this form of the fourth Routh–Hurwitz criterion for model II(s) is necessary and sufficient to guarantee that the infected equilibrium of model II(s) is locally stable.

Appendix B. Eigenvalues of the connectivity matrix for a Moore neighborhood

The geometry of the dispersal neighborhood in spatially structured models can be encoded in a connectivity matrix C. If we assume that connectedness of a site with another one is a symmetric relation, then C is real and symmetrical. It is built from $n \times n$ submatrices A, B, and 0, which in the case of periodic boundary conditions have a circulant structure

$$C = \begin{pmatrix} A & B & 0 & \cdots & 0 & B \\ B & A & B & \ddots & \vdots & 0 \\ 0 & B & A & \ddots & 0 & \vdots \\ \vdots & \ddots & \ddots & \ddots & B & 0 \\ 0 & \cdots & 0 & B & A & B \\ B & 0 & \cdots & 0 & B & A \end{pmatrix}. \qquad \text{(B.1)}$$

For example, the $n \times n$ matrix A that forms the entries in the diagonal of C has the following structure:

$$A = \begin{pmatrix} -8 & 1 & 0 & \cdots & 0 & 1 \\ 1 & -8 & 1 & \ddots & \vdots & 0 \\ 0 & 1 & -8 & \ddots & 0 & \vdots \\ \vdots & \ddots & \ddots & \ddots & 1 & 0 \\ 0 & \cdots & 0 & 1 & -8 & 1 \\ 1 & 0 & \cdots & 0 & 1 & -8 \end{pmatrix}. \qquad \text{(B.2)}$$

The $n \times n$ matrix B, which appears in the super- and subdiagonal of C as well as in the upper right-hand corner and the lower left-hand corner, has the following structure:

$$B = \begin{pmatrix} 1 & 1 & 0 & \cdots & 0 & 1 \\ 1 & 1 & 1 & \ddots & \vdots & 0 \\ 0 & 1 & 1 & \ddots & 0 & \vdots \\ \vdots & \ddots & \ddots & \ddots & 1 & 0 \\ 0 & \cdots & 0 & 1 & 1 & 1 \\ 1 & 0 & \cdots & 0 & 1 & 1 \end{pmatrix}. \qquad \text{(B.3)}$$

Finally, a $n \times n$ nullmatrix 0 is also required to built up the $n^2 \times n^2$ connectivity matrix C.

The eigenvalues of a circulant matrix are well known and can be found, e.g. in Othmer and Scriven (1971, p. 517f). The formula for the eigenvalues μ_{kl} of the connectivity matrix C describing connectedness of a site with its eight adjacent sites (Moore neighborhood) on a regular two-dimensional grid follows from the following statement:

$$\mu_{kl} = [1 + 2\cos(2\pi k/n)][1 + 2\cos(2\pi l/n)] - 9, \qquad \text{(B.4)}$$

which, after some trigonometric transformations, leads to the following expression:

$$\mu_{kl} = 2(2\cos(2\pi k/n) + \cos(4\pi l/n) - 3), \qquad \text{(B.5)}$$

with $k = 0, 1, \ldots, n-1$ and $l = 0, 1, \ldots, n-1$. Because C is a real, symmetrical matrix, all of its eigenvalues must be real numbers as well. As one can see from formula (B.5), the dominant eigenvalue of C is zero while its smallest eigenvalue is achieved when both cosine terms take the value –1, leading to $\mu_{kl} = -12$. Hence $\mu_{kl} \in [-12, 0]$.

References

Ambrose, Z., Larsen, K., Thompson, J., Stevens, Y., Finn, E., Hu, S.-L., Bosch, M.L., 2001. Evidence for early local viral replication and local production of antiviral immunity upon mucosal simian-human immunodeficiency virus SHIV89.6 infection in Macaca nemestrina. J. Virol. 75, 8589–8596.

Anderson, D.H., 1983. Compartmental Modeling and Tracer Kinetics. Springer.

Anderson, R.M., May, R.M., 1991. Infectious Diseases of Humans. Oxford University Press.

Bonhoeffer, S., May, R.M., Shaw, G.M., Nowak, M.A., 1997. Virus dynamics and drug therapy. Proc. Natl Acad. Sci. USA 94, 6971–6976.

Bourinbaiar, A.S., Phillips, D.M., 1991. Transmission of human immunodeficiency virus from monocytes to epithelia. J. Acquir. Immune Defic. Syndr. 45, 56–63.

Callaway, D., Perelson, A.S., 2002. HIV-1 infection and low steady state viral loads. Bull. Math. Biol. 64, 29–64.

Cheynier, R., Henrichwark, S., Hadida, F., Pelletier, E., Oksenhendler, E., Autran, B., Wain-Hobson, S., 1994. HIV and T cell expansion in splenic white pulps is accompanied by infiltration of HIV-specific cytotoxic T lymphocytes. Cell 78, 373–387.

Chun, T.-W., Carruth, L., Finzi, D., Shen, X., DiGiuseppe, J.A., Taylor, H., Hermankova, M., Chadwick, K., Margolick, J.B., Quinn, T.C., Kuo, Y.H., Brookmeyer, R., Zeiger, M.A., Barditch-Crovo, P., Siliciano, R.F., 1997. Quantification of latent tissue reservoirs and total body viral load in HIV-1 infection. Nature 387, 183–188.

Dias, P.C., 1996. Sources and sinks in population biology. Trends Ecol. Evol. 11, 326–330.

Emery, V.C., Cope, A.V., Bowen, E.F., Gor, D., Griffiths, P.D., 1999. The dynamics of human cytomegalovirus replication in vivo. J. Exp. Med. 190, 177–182.

Emery, V.C., Hassan-Walker, A.F., Burroughs, A.K., Griffiths, P.D., 2002. Human cytomegalovirus (HCMV) replication dynamics in HCMV-naïve and -experienced immunocompromised hosts. J. Infect. Dis. 185, 1723–1728.

Funk, G.A., 2003. Models of human immunodeficiency virus type I infection: exploring viral fitness, cytopathicity and spatial structure. Dissertation ETH No. 14967 (Ph.D. Thesis).

Funk, G.A., Fischer, M., Joos, B., Opravil, M., Gunthard, H.F., Ledergerber, B., Bonhoeffer, S., 2001. Quantification of in vivo replicative capacity of HIV-1 in different compartments of infected cells. J. Acquir. Immune Defic. Syndr. 26, 397–404.

Frost, S.D., Dumaurier, M.-J., Wain-Hobson, S., Leigh Brown, A.J., 2001. Genetic drift and within-host metapopulation dynamics of HIV-1 infection. Proc. Natl Acad. Sci. USA 98, 6975–6980.

Gaylord, R.J., Nishidate, K., 1996. Modelling Nature: Cellular Automata Simulations with Mathematica. Springer, New York.

Gratton, S., Cheynier, R., Dumaurier, M.-J., Oksenhendler, E., Wain-Hobson, S., 2000. Highly restricted spread of HIV-1 and multiply infected cells within splenic germinal centers. Proc. Natl Acad. Sci. USA 97, 14556–14571.

Grossman, Z., Feinberg, M.B., Paul, W.E., 1998. Multiple modes of cellular activation and virus transmission in HIV infection: a role for chronically and latently infected cells in sustaining viral replication. Proc. Natl Acad. Sci. USA 95, 6314–6319.

Gueye, A., Diop, M.O., Ploquin, M.J.Y., Kornfeld, C., Faye, A., Cumont, M.-C., Hurtel, B., Barré-Sinoussi, F., Müller-Trutwin, M.C., 2004. Viral load in tissues during early and chronic phase of non-pathogenic SIVagm infection. J. Med. Primatol. 33, 83–97.

Haase, A.T., Henry, K., Zupancic, M., Sedgewick, G., Faust, R.A., Melroe, H., Cavert, W., Gebhard, K., Staskus, K., Zhang, Z.Q., Dailey, P.J., Balfour, H.H., Erice, A., Perelson, A.S., 1996. Quantitative image analysis of HIV-1 infection in lymphoid tissue. Science 274, 985–989.

Hassell, M.P., Comins, H.N., May, R.M., 1991. Spatial structure and chaos in insect population dynamics. Nature 353, 255–258.

Hengel, H., Brune, W., Koszinowski, U.H., 1998. Immune evasion by cytomegalovirus survival strategies of a highly adapted opportunist. Trends Microbiol 6, 190–197.

Ho, D.D., Neumann, A.U., Perelson, A.S., Chen, W., Leonard, J.M., Markowitz, M., 1995. Rapid turnover of plasma virions and CD4 lymphocytes in HIV-1 infection. Nature 373, 123–126.

Huang, A.Y., Qi, H., Germain, R.N., 2004. Illuminating the landscape of in vivo immunity; insights from dynamic in situ imaging of secondary lymphoid tissues. Immunity 21, 331–339.

Jacquez, J.A., 1985. Compartmental Analysis in Biology and Medicine. The University of Michigan Press, Ann Arbor.

Jansen, V.A.A., Lloyd, A.L., 2000. Local stability analysis of spatially homogeneous solutions of multi-patch systems. J. Math. Biol. 41, 232–252.

Johnson, D.C., Huber, M.T., 2002. Directed egress of animal viruses promotes cell-to-cell spread. J. Virol. 76, 1–8.

Kaul, R., Plummer, F.A., Kimani, J., Dong, T., Kiama, P., Rostron, T., Njagi, E., MacDonald, K.S., Bwayo, J.J., McMichael, A.J., Rowland-Jonesw, S.L., 2000. HIV-1-specific mucosal CD8+ lymphocyte responses in the cervix of HIV-1-resistant prostitutes in Nairobi. J. Immunol. 164, 1602–1611.

Lam, N.P., Neumann, A.U., Gretch, D.R., Wiley, T.E., Perelson, A.S., Layden, T.J., 1997. Dose-dependent acute clearance of hepatitis C genotype 1 virus with interferon alfa. Hepatology 26, 226–231.

Lau, G.K., Yuen, S.T., Au, W.Y., Wu, P.C., Liang, R., 1999. Histological changes during clearance of chronic hepatitis B virus infection by adoptive immunity transfer. J. Gastroenterol. Hepatol. 14, 262–268.

Levin, A.S., 1974. Dispersal and population interactions. Am. Nat. 108, 207–228.

Levins, R., 1969. Some demographic and genetic consequences of environmental heterogeneity for biological control. Bull. Entomol. Soc. Am. 15, 237–240.

Lindback, S., Karlsson, A.C., Mittler, J., Blaxhult, A., Carlsson, M., Briheim, G., Soennerborg, A., Gaines, H., 2000. for the Karolinska Institute Primary HIV Infection Study Group, Viral dynamics in primary HIV-1 infection. AIDS 14, 2283–2291.

Little, S., McLean, A.R., Spina, C.A., Richmann, D.D., Havlir, D.V., 1999. Viral dynamics of acute HIV-1 infection. J. Exp. Med. 190, 841–850.

Lloyd, A.L., Jansen, V.A.A., 2004. Spatiotemporal dynamics of epidemics: synchrony in metapopulation models. Math. Biosci. 188, 1–16.

Mandl, S., Schimmelpfennig, C., Edinger, M., Negrin, R.S., Contag, C.H., 2002. Understanding immune cell trafficking patterns via in vivo bioluminescence imaging. J. Cell. Biochem. Suppl. 39, 239–248.

May, R.M., 1974. Stability and Complexity in Model Ecosystems. Princeton University Press, Englewood Cliff, NJ.

Miller, S.E., Levenson, R.M., Aldridge, C., Hester, S., Kenan, D.J., Howell, D.N., 1997. Identification of focal viral infections by confocal microscopy for subsequent ultrastructural analysis. Ultrastruct. Pathol. 21, 183–193.

Minc, H., 1988. Nonnegative Matrices. John Wiley, New York.

Neumann, A.U., Lam, N.P., Dahari, H., Gretch, D.R., Wiley, T.E., Layden, T.J., Perelson, A.S., 1998. Hepatitis C viral dynamics in vivo and the antiviral efficacy of interferon-α therapy. Science 282, 103–107.

Nowak, M.A., Bangham, C.R.M., 1996. Population dynamics of immune responses to persistent viruses. Science 272, 74–79.

Nowak, M.A., May, R.M., 2000. Virus Dynamics: Mathematical Principles of Immunology and Virology. Oxford University Press, Oxford.

Nowak, M.A., May, R.M., Sigmund, K., 1995. Immune responses against multiple epitopes. J. Theor. Biol. 175, 325–353.

Nowak, M.A., Bonhoeffer, S., Hill, A.M., Boehme, R., Thomas, H.C., McDade, H., 1996. Viral dynamics in hepatitis B virus infection. Proc. Natl Acad. Sci. USA 93, 4398–4402.

Nowak, M.A., Lloyd, A.L., Vasquez, G.M., Wiltrout, T.A., Wahl, L.M., Bischofberger, N., Williams, J., Kinter, A., Fauci, A.S., Hirsch, V.S., Lifson, J.D., 1997. Viral dynamics of primary viremia

and antiretroviral therapy in simian immunodeficiency virus infection. J. Virol. 71, 7518–7524.

Othmer, G.H., Scriven, L.E., 1971. Instability and dynamic pattern in cellular networks. J. Theor. Biol. 32, 507–537.

Pantaleo, G., Graziosi, C., Fauci, A.S., 1993. The role of lymphoid organs in the pathogenesis of HIV infection. Semin. Immunol. 5, 157–163.

Payne, R.J., Nowak, M.A., Blumberg, B.S., 1996. The dynamics of hepatitis B virus infection. Proc. Natl Acad. Sci. USA 93, 6542–6546.

Perelson, A.S., Neumann, A.U., Markowitz, M., Leonard, J.M., Ho, D.D., 1996. HIV-1 dynamics in vivo: virion clearance rate, infected cell life-span, and viral generation time. Science 271, 1582–1586.

Perelson, A.S., Essunger, P., Cao, Y., Vesanen, M., Hurley, A., Saksela, K., Markowitz, M., Ho, D.D., 1997. Decay characteristics of HIV-1 infected compartments during drug combination therapy. Nature 387, 188–191.

Phillips, A.N., 1996. Reduction of HIV concentration during acute infection: independence from a specific immune response. Science 271, 497–499.

Ramratnam, B., Bonhoeffer, S., Binley, J., Hurley, A., Zhang, L., Mittler, J.E., Markowitz, M., Moore, J.P., Perelson, A.S., Ho, D.D., 1999. Rapid production and clearance of HIV-1 and hepatitis C virus assessed by large volume plasma apheresis. Lancet 354, 1782–1785.

Reinhart, T.A., Rogan, M.J., Amedee, A.M., Murphey-Corb, M., Rausch, D.M., Eiden, L.E., Haase, A.T., 1998. Tracking members of the simian immunodeficiency virus delta b670 quasispecies population in vivo at single-cell resolution. J. Virol. 72, 113–120.

Sprent, J., Tough, D.F., 1994. Lymphocyte lifespan and memory. Science 265, 1395–1400.

Strain, M.C., Richman, D.D., Wong, J.K., Levine, H., 2002. Spatiotemporal dynamics of HIV propagation. J. Theor. Biol. 218, 85–96.

Tan, X., Pearce-Pratt, R., Phillips, M.D., 1993. Productive infection of a cervical epithelial cell line with human immunodeficiency virus: implications for sexual transmission. J. Virol. 67, 6447–6452.

Tibaldi, E.V., Salgia, R., Reinherz, E.L., 2002. CD2 molecules redistribute to the uropod during T cell scanning: implications for cellular activation and immune surveillance. Proc. Natl Acad. Sci. USA 99, 7582–7587.

Wei, X., Ghosh, S.K., Taylor, M.E., Johnson, V.A., Emini, E.A., Deutsch, P., Lifson, J.D., Bonhoeffer, S., Nowak, M.A., Hahn, B.H., Saag, M.S., Shaw, G.S., 1995. Viral dynamics in human immunodeficiency virus type 1 infection. Nature 373, 117–123.

Whalley, S.A., Murray, J.M., Brown, D., Webster, G.J.M., Emery, V.C., Dusheiko, G.M., Perelson, A.S., 2001. Kinetics of acute hepatitis B virus infection in humans. J. Exp. Med. 193, 847–853.

Wodarz, D., May, R.M., Nowak, M.A., 2000. The role of antigen-independent persistence of memory cytotoxic T lymphocytes. Int. Immunol. 12, 467–477.

Zeuzem, S., Schmidt, J.M., Lee, J.-H., Ruster, B., Roth, W.K., 1996. Effect of interferon alfa on the dynamics of hepatitis C virus turnover. Hepatology 23, 366–371.

Zorzenon dos Santos, R.M., Coutinho, S., 2001. Dynamics of HIV infection: a cellular automata approach. Phys. Rev. Lett. 87, 168102.